Soft Matter

Cite this: *Soft Matter*, 2011, **7**, 10967

www.rsc.org/softmatter

PAPER

Deformation and clustering of red blood cells in microcapillary flows†

J. Liam McWhirter,[a] Hiroshi Noguchi[ab] and Gerhard Gompper*[a]

Received 1st May 2011, Accepted 5th August 2011
DOI: 10.1039/c1sm05794d

The shape changes and clustering of red blood cells (RBCs) under flow in cylindrical microcapillaries are studied using a triangulated surface model for the membrane and a particle-based mesoscopic simulation technique for the embedding fluid. As the flow velocity increases, the RBCs make a transition from a discocyte shape at low velocities to a parachute shape at high velocities; close to the critical flow velocity, the RBC can also be found in a transient slipper shape. The transition and critical flow velocity are examined for various capillary diameters and RBC volume fractions (hematocrit H_T). At high flow velocities and low hematocrits, the parachute-shaped RBCs can be found in clusters which are hydrodynamically stabilized. Here, the formation of a fluid vortex between neighboring cells, called bolus, develops which keeps the cells at a preferred distance. Decreasing the flow velocity towards the critical velocity, we observe an increasing frequency of drastic RBC shape fluctuations to slipper-shaped RBCs that can result in cluster breakup. These clusters resemble those seen in experiments using optical microscopy.

1 Introduction

The flow of blood through arteries, arterioles and capillaries, the heart and the lungs, is of paramount importance for humans and other vertebrate animals. Therefore, the understanding of the complex physical and biochemical processes in blood flow and oxygen transport, and their disruption due to injuries or illnesses, has many medical implications, and poses many scientific challenges.

We want to focus here on a particular aspect of blood flow: the pressure-driven flow through narrow capillaries, where the capillary diameter is comparable to the diameter of the red blood cells. In general, soft objects such as liquid droplets, lipid vesicles, and red blood cells (RBCs) show complex behavior in flow because they have long structural relaxation times and exhibit large deformation due to shear forces. Examples are the break-up of droplets[1] and the wrinkling of elastic capsules[2,3] or lipid vesicles[4,5] in shear flows, and the deformation of lipid vesicles[6] and RBCs[7–10] into parachute shapes in capillary flows.

In the absence of flow, human RBCs have a biconcave-disc shape, whose maximum diameter and thickness are about 7.6 μm and 2 μm with constant area S and volume V.[11] The RBC membrane consists of a lipid bilayer supported by an attached spectrin network that acts as a cytoskeleton. The bilayer resistance to bending is controlled by curvature elasticity with a bending rigidity, κ; the spectrin's resistance to a shear strain is characterized by a shear modulus, μ. Measurements by micropipette aspiration[12] and stretching by optical tweezers[13] imply $\kappa/k_BT \simeq 50$ and $\mu R_0^2/k_BT \simeq 10^4$ under physiological conditions,[11,14] where $R_0 = 3.3$ μm is the average RBC radius. An RBC has a large surface area-to-volume ratio and a small bending rigidity, so that it is easily deformable. This deformability has the important physiological implication that an RBC is able to change its shape to move through extremely narrow blood vessels and capillaries with diameters as small as 2 μm,[15,16] much less than the maximum diameter of the RBC.

Because the deformability of RBCs is reduced in diseases such as diabetes mellitus[10] and sickle cell anemia,[17] and in infections such as malaria,[15] it is important to understand the effect of membrane elasticity on the flow behavior. Recently, it has been found that RBC deformation also induces ATP release from RBCs, which induces nitric oxide synthesis and results in an increase of the vascular caliber.[18,19] Thus, the shape deformation of RBCs in microvessels is very important to regulate oxygen delivery.

Two interesting, related effects have been observed with blood flow through blood vessels or glass tubes when these capillary diameters are decreased from about 0.3 mm to about 10 μm. The apparent (or effective) viscosity of the blood decreases; in addition, the hematocrit ratio H_T/H_D decreases, where H_T and H_D are the volume fraction of RBCs in capillary (tube) and in the suspension collected at the end of the tube (discharge), respectively. These two effects are known as the Fåhraeus–Lindqvist and Fåhraeus effects, respectively.[20,21] Both effects are now understood to be a result of lift forces that drive the RBCs away

[a]*Theoretical Soft Matter and Biophysics, Institute of Complex Systems, Forschungszentrum Jülich, 52425 Jülich, Germany. E-mail: j.mcwhirter@fz-juelich.de; g.gompper@fz-juelich.de*
[b]*Institute for Solid State Physics, University of Tokyo, Kashiwa, Chiba, 277-8581, Japan. E-mail: noguchi@issp.u-tokyo.ac.jp*
† Electronic supplementary information (ESI) available. See DOI: 10.1039/c1sm05794d

from the capillary wall towards the capillary center, producing a plasma skimming layer free of RBCs by the wall.[22] As the diameter of the capillary decreases, the relative ratio of the cross-sectional area of this cell-free layer increases. The hematocrit $H_T \simeq 0.1$–0.2 observed in human microvessels is much lower than the average hematocrit $H \simeq 0.45$ for whole blood, as a consequence of the Fåhraeus effect and the unequal partitioning of RBCs and plasma at vessel bifurcations.[11] The RBC density in microvessels is strongly fluctuating.

Theoretical studies have focused on the effects of cell spacing in narrow capillaries where the capillary radius is comparable to the radius of RBCs. If the vessel diameter is decreased below 10 μm, the apparent/effective viscosity begins to increase. This phenomenon is called the inverse Fåhraeus–Lindqvist effect. The earliest theoretical model of RBCs in a narrow capillary flow, the axial-train or stacked-coin model,[23] which employed the lubrication approximation for a regular array of cylindrically shaped cells and piecewise-parabolic flow profiles, reproduced this experimentally observed effect qualitatively. Later studies involved the solution of the Stokes equation for the fluid flow about a periodic (equally spaced) array of model cells.[24–27] The cells were modeled as rigid, non-deformable spheres, spheroids, cylinders, and discocytes. The results were qualitatively independent of cell shape. The relative apparent viscosity (relative to a fluid free of cells) was found to increase with increasing hematocrit and with decreasing capillary diameter, as can be expected intuitively. The additional pressure drop per cell becomes independent of the cell-to-cell distance once this distance becomes larger than the capillary diameter; in other words, once the cells are spaced at a distance of one capillary diameter or more, they become 'hydrodynamically independent' (or 'hydrodynamically isolated'). Thus, confinement screens long-range hydrodynamic interactions between immersed cells or colloids, effectively reducing the range of these interactions to the diameter of the confining vessel.[28,29] When the cells are close to each other, the flow approaches the truncated Poiseuille flow of the stacked-coins model.[30]

As mentioned above, human RBCs are not fixed in shape, but are highly deformable. Recent theoretical efforts have been devoted to understanding the shape changes of RBCs in narrow capillaries, both by applying the lubrication approximation[30–32] and by employing several numerical simulation techniques.[33–39] To treat the no-slip boundary conditions and the impenetrability of the moving cell surface, boundary integral methods,[33–35] immersed-boundary methods,[36,37] or particle-based methods[38–40] have been developed.

We employ here a particle-based hydrodynamics technique, called Multi-Particle Collision dynamics (MPC),[41–43] to describe the embedding fluid. This method shares many properties with other particle-based methods.[44] The most widely used version of MPC is also called Stochastic Rotation Dynamics (SRD).[45] The MPC method has been employed previously to study the dynamics of a single fluid vesicle in shear flow,[46–48] and a fluid vesicle[39,49] as well as an RBC[39] in capillary flow. Recently, we extended this study to multiple RBCs; the simulations showed that hydrodynamic interactions between RBCs can induce ordered RBC arrangements in dense suspensions, and clustering in dilute suspensions.[50]

In this paper, we pursue two objectives. First, we determine the dependence of the shape transition—from discocyte to parachute—of a model RBC in a cylindrical capillary on the capillary radius and the fluid hematocrit (Sec. 3). Then, we examine the formation of clusters of RBCs in a dilute suspension of RBCs (Sec. 4). We consider only the hydrodynamic interaction and excluded-volume repulsion between RBCs, but exclude attractive interactions and depletion effects; this corresponds to RBC suspensions without fibrinogen and other plasma proteins which induce RBC aggregation.[51]

2 Model and methods

We combine a particle-based hydrodynamics simulation technique, multi-particle collision dynamics (MPC),[41–43] of the embedding fluid with dynamically-triangulated surface model of the membrane.[52,53] We provide here a brief summary of the model and the simulation method; a detailed account has been given elsewhere.[39,47]

2.1 Membrane model

Each membrane is modeled as a collection of $N_{mb} = 500$ vertices of mass m_{mb}, interconnected by two triangular networks of bonds:[54,55] a network of fixed connectivity whose bonds are harmonic springs, and a dynamically-triangulated network whose bonds undergo 'flips'. The elastic network of fixed connectivity models the spectrin cytoskeleton of a real RBC, while the dynamic network models the fluid lipid bilayer. We refer to these model RBCs as 'elastic vesicles' below. The spring constant, k_{el} of the harmonic bonds generates a shear modulus $\mu = \sqrt{3}k_{el}$. In the fluid network, the fluctuations and shape changes of the membrane are controlled by the curvature elasticity with the Hamiltonian[56]

$$U_{cv} = (\kappa/2)\int (C_1 + C_2)^2 \mathrm{d}S, \qquad (1)$$

where κ is the bending rigidity, and C_1 and C_2 are the principal curvatures at each point of the membrane. The curvature energy is discretized using dual lattices.[47,57] We employ $\kappa = 20k_BT$ which is the rigidity of typical phospholipid membranes, where k_BT is the thermal energy. Different patches of the RBC membrane experience a short-range repulsion, which is modeled by an excluded-volume interaction of membrane vertices, whether bonded or not, such that the minimum distance between any two vertices on a given membrane is $l_{min} = 0.67\ell$, where ℓ is the maximum bond length. In addition, global volume and local area constraint potentials are added that keep the volume V and global area S of the membrane fixed within less than 1% deviation.[47] The reduced volume of a given RBC is $V^* = V/(4\pi R_0^3/3) = 0.59$, where $R_0 = \sqrt{S/4\pi}$ is the radius of a sphere with the same surface area S; for this volume, the stable shape of the fluid vesicle at thermal equilibrium (no fluid flows or other external fields) is a biconcave discocyte. For an RBC, this effective radius is $R_0 = 3.3$ μm.[58,59] In order to establish the connectivity of the spectrin mesh, we initially perform simulations of a fluid vesicle with the same reduced volume; after equilibration, the elastic bonds are added between neighbors defined by the fluid bonds of this particular conformation. Note that the elastic bonds have zero rest length, which implies that the spectrin network is under tension; however, this tension is

balanced to a large extent by the incompressibility of the fluid membrane network. The shear modulus of the elastic vesicle is set to $\mu R_0^2/k_BT = 110$.

The membrane vertices of different RBCs have a repulsive interaction given by an excluded-volume potential[47] where the minimum distance between vertices is $l_{min} = 0.77\ell$. This minimum distance is somewhat larger than that between two vertices on the same membrane ($l_{min} = 0.67\ell$) to prevent interpenetration of two neighboring cells.

2.2 Multi-particle-collision dynamics (MPC)

The MPC fluid[41–43] is modeled by N_s point particles of mass m_s. The dynamics of MPC consists of series of two alternating steps: a free-streaming step with time step Δt_{CD}, where the fluid particles move ballistically, followed by a collision step, where the fluid particles locally exchange their momenta. During the latter step, the particles are first sorted into cubic boxes with lattice constant a; then for particles in a given collision box, the particle velocities, relative to the center-of-mass (cm) velocity of the box, are rotated through an angle of $\pi/2$ about an axis chosen randomly for each box. During a collision, the total momentum and kinetic energy of each box are conserved; consequently, MPC describes hydrodynamic flows of a Newtonian fluid. A velocity-rescaling thermostat for relative velocities in each collision box is added to the dynamics to extract the heat generated by the shear gradients under flow. We investigate blood flow in capillaries with radii R_{cap} in the range $R_{cap}/R_0 = 1.23$ to 1.75. For the capillaries with the two largest diameters, a velocity rescaling is performed for rectangular bins of size $a \times a \times L_z$, where L_z is the length of the capillary (which is taken to be oriented in the z-direction). For the smaller capillary diameters, a global velocity rescaling is employed. The position of the collision-box lattice is shifted randomly before each collision step to ensure Galilean invariance.[45]

The particles of the MPC fluid interact with the capillary walls *via* a 'bounce-back' rule that produces no-slip or stick boundaries.[60] The fluid particles interact with the membranes during the streaming step also *via* a bounce-back rule that scatters fluid particles off the membrane triangles (fluid network) thereby preventing the fluid from the exterior of the membrane to penetrate into the interior and *vice versa*.[47] In addition, the membrane vertices interact with the interior and exterior fluids through MPC collisions.

2.3 Parameters

To obtain low Reynolds numbers and large Schmidt numbers,[61] we employ a small collision time step $\Delta t_{CD} = 0.025a\sqrt{m_s/k_BT}$. With a fluid mass density of $\rho = 10m_s/a^3$, the shear viscosity of the fluid is $\eta_0 = 20.1\sqrt{m_sk_BT}/a^2$. This guarantees that the capillary Reynolds number is $Re \leq 10^{-2}$ for all our flow simulations.

For the membrane, we use the vertex mass $m_{mb} = 10m_s$ and the bond length $\ell = a$. This implies $V = 450a^3$, $S = 407a^2$, and $R_0 = 5.7a$. To integrate the membrane dynamics using a molecular dynamics algorithm, we employ a shorter time step $\Delta t_{MD} = \Delta t_{CD}/20 = 0.00125a\sqrt{m_s/k_BT}$.

We performed simulations of single ($n_{ves} = 1$) and several ($n_{ves} = 3$ and $n_{ves} = 6$) elastic vesicles in a cylindrical capillary of radius R_{cap} with various cylinder lengths L_z, where periodic boundary conditions are used along the flow direction, and n_{ves} is the number of cells in the capillary. In reporting our results, we have scaled lengths by the RBC radius R_0, energy by κ, and time by $\tau = \eta_0R_0^3/\kappa$. Reduced variables are denoted by an asterisk superscript, such that, *e.g.*, $L_z^* = L_z/R_0$. Flow is driven by a uniform external force g on each particle in the z direction, which is equivalent to a pressure gradient $\nabla_z P = -\rho_m g$. Employing this external force has the advantage of minimizing density gradients in the MPC fluid. In our reduced units, the force strength is

$$g^* = \rho_m g R_0^4/\kappa. \quad (2)$$

In the absence of RBCs, this external field generates an average fluid velocity $v_m = \rho g R_{cap}^2/8\eta_0$, *i.e.* the flow velocity increases linearly with g^*. The error bars are calculated from several independent simulation runs that started from different initial conditions and employ different realizations of the thermal noise.

3 Shape transitions of a regular array of RBCs

3.1 Shape transitions of an isolated RBC

We first describe the shape changes and dynamics of a single elastic vesicle ($n_{ves} = 1$) in a dilute cell suspension within a long capillary cylinder, $L_z/R_0 = 14$, at various capillary radii, from $R_{cap}/R_0 = 1.23$ to $R_{cap}/R_0 = 1.75$, which corresponds to the range of capillary radii $R_{cap} = 4.0$ μm to $R_{cap} = 5.8$ μm, and hematocrits $H_T = V_{ves}/(\pi R_{cap}^2 L_z)$ from $H_T = 0.037$ to $H_T = 0.018$, respectively. The considered tube segment is sufficiently long that the cell is effectively isolated hydrodynamically from its periodic images. In the absence of flow, the RBC appears as a biconcave discocyte. At low flow velocities, or equivalently low g^*, the RBC retains its discocyte and moves 'edge-on' through the capillary, *i.e.* it orients in the direction of flow so that the eigenvector associated with the smallest eigenvalue of the cell's gyration tensor becomes roughly perpendicular to the direction of flow.[39] This orientation offers the least blockage or resistance to the capillary flow since it minimizes the area of the elastic vesicle projected onto the capillary cross-section. If the flow velocity or g^* is sufficiently high, then the RBC undergoes a sudden transition[39] into a parachute shape at a critical value, g_c^*, as shown in Fig. 1. This parachute shape is in good agreement with the RBC shape observed by optical microscopy.[7–10,62]

The flow profile of the fluid far from a cell approaches the Poiseuille flow, $v(r) = \rho g(R_{cap}^2 - r^2)/4\eta_0$, where r is the radial distance in cylindrical coordinates from the capillary axis. The shape transition of the RBC is driven by the gradients in the fluid flow, $dv/dr = -\rho gr/2\eta_0$, which is independent of R_{cap}. Therefore, for sufficiently large capillary radii, when the backflow from the wall and thus hydrodynamic interactions with the wall become negligible, the critical pressure gradient g_c^* should become independent of R_{cap}. This is seen in Fig. 1, where g_c^* reaches a plateau value $g_c^* \simeq 9.45$ for $R_{cap}/R_0 \gtrsim 1.55$. Although g_c^* reaches a plateau with increasing R_{cap}, the mean flow velocity does not, because the mean velocity of Poiseuille flow increases as $v_m = \rho g R_{cap}^2/8\eta_0$. It is interesting to note that for $R_{cap} < 1.55R_0$, a *smaller* pressure gradient is sufficient to induce the transformation to parachute shapes than for wide capillaries.

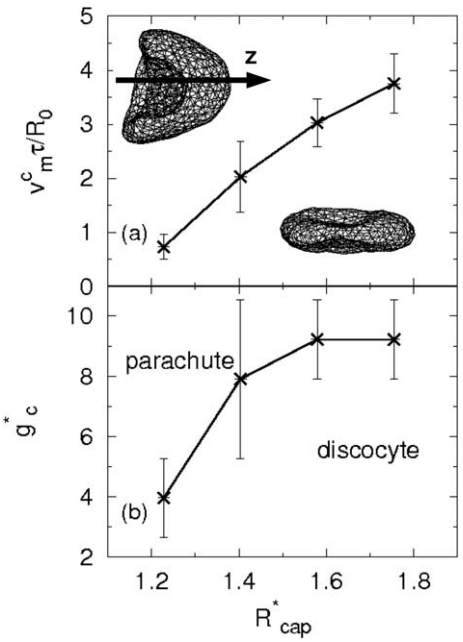

Fig. 1 Dependence of the shape-transition (a) mean flow velocity, v_m^c, and (b) uniform pressure gradient, g_c^*, on the capillary radius, R_{cap}/R_0, for a dilute suspension with $n_{ves} = 1$ and $L_z^* = L_z/R_0 = 14$. Simulation snapshots of a discocyte and parachute are included.

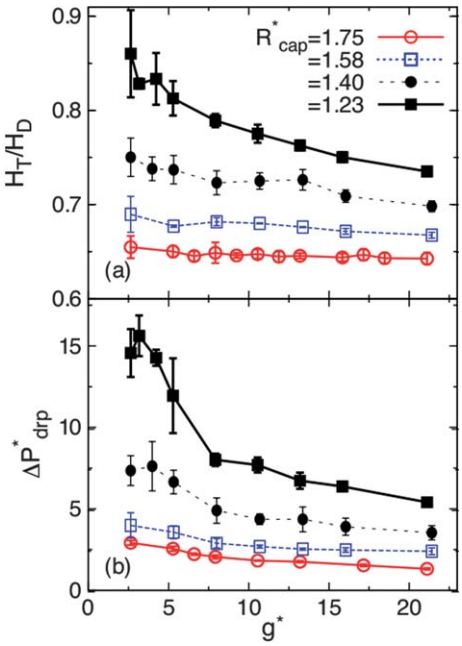

Fig. 2 (a) Hematocrit ratio, $H_T/H_D = v_{ves}/v_m$, and (b) pressure drop, $\Delta P^*_{drp} = \Delta P_{drp}R^2_{cap}/(\eta_0 v_m R_0)$, as a function of the pressure gradient, g^*, for capillaries of different radii, R_{cap}/R_0, with $n_{ves} = 1$ and $L_z/R_0 = 14$.

The pressure drop ΔP_{drp} is the additional pressure difference required to maintain the flow with RBCs at the same mean flow velocity v_m as in a fluid without RBCs. Across a section of capillary or pipe of length L_z, the pressure drop is given by

$$\frac{\Delta P_{drp} R_{cap}^2}{\eta_0 v_m R_0} = \frac{8(v_0 - v_m)L_z}{n_{ves} v_m R_0}, \quad (3)$$

where v_0 is the mean flow velocity in a capillary without RBCs that is generated by the same uniform pressure gradient.

Fig. 2 shows that the hematocrit ratio $H_T/H_D = v_m/v_{ves}$ and the pressure drop ΔP_{drp} decrease rapidly with increasing g^* around g_c^* for the narrowest capillary with $R_{cap}/R_0 = 1.23$, but much more gradually for $R_{cap}/R_0 \geq 1.40$. Since the RBC stays more compact around the center of the capillary after the transformation into a parachute shape, it flows faster than the mean blood velocity v_m, thereby lowering H_T, and significantly reducing the resistance to fluid flow.

The stretching energy of the elastic bond network and the bending energy of the fluid membrane both increase with increasing g^*; the bending energy of the fluid membrane increases sharply at the discocyte-to-parachute transition. To determine g_c^*, we also inspected movies of the RBC under flow with many different initial conformations; these runs typically covered $10^2\tau$ in time. Around the transition velocity, the RBC can also assume a transient non-axisymmetric 'slipper' shape.[39] No stable slipper shapes were observed, in contrast to results for two-dimensional vesicles in planar unbounded Poiseuille flow (in the absence of thermal fluctuations).[63]

Previously, the transition velocity v_m^c to a parachute was found to depend linearly on the elastic bending and stretching forces,[39] with

$$v_m^c\tau/R_0 = 0.05\mu R_0^2/\kappa + 2 \quad (4)$$

at $R_{cap}/R_0 = 1.40$ in a dilute suspension. The extrapolation suggests that the transition occurs at 0.2 mm s^{-1} for the bending and shear modulus of RBCs, under physiological conditions in capillaries with $R_{cap} = 4.6$ μm. We expect a similar linear dependence on μ and κ; however, the transition velocity also depends on R_{cap} as shown in Fig. 1, so that the coefficients must be (slowly) varying functions of R_{cap}.

3.2 Shape transitions of RBCs at higher hematocrits

We can also study the effect of hydrodynamic interactions between neighboring cells in a regular array on the RBC shape and orientation at higher hematocrit by simulating a *single* RBC ($n_{ves} = 1$) in a tube with periodic boundary conditions—as long as the shapes, orientations, and neighbor distances of the cells are all the same. We investigate the dependence on the hematocrit in the range $0.1 \leq H_T \leq 0.4$ by varying the capillary length L_z (per cell) at fixed radius $R_{cap}/R_0 = 1.40$. At low $H_T \lesssim 0.19$ (or $L_z/R_0 \gtrsim 2$), the transition from a discocyte to a parachute occurs abruptly with increasing g^*. However, at high $H_T \gtrsim 0.19$ (or $L_z/R_0 \lesssim 2$), the shape transition is gradual; starting at low g^* as a discocyte whose symmetry axis is tilted away from the capillary axis, the RBC shape changes gradually with increasing g^*, proceeding through a shape similar to a slipper whose degree of deformation away from the discocyte shape increases becoming a bowl at high g^*. The deviation from a spherical shape can be characterized by the average asphericity, $\langle\alpha\rangle$, with[47,64]

$$\alpha = \frac{(\lambda_1 - \lambda_2)^2 + (\lambda_2 - \lambda_3)^2 + (\lambda_3 - \lambda_1)^2}{2R_g^4}, \quad (5)$$

where $\lambda_1 \leq \lambda_2 \leq \lambda_3$ are the eigenvalues of the gyration tensor and $R_g^2 = \lambda_1 + \lambda_2 + \lambda_3$ is the squared radius of gyration. Results are shown in Fig. 3. The critical value of H_T (between 0.16 and 0.22),

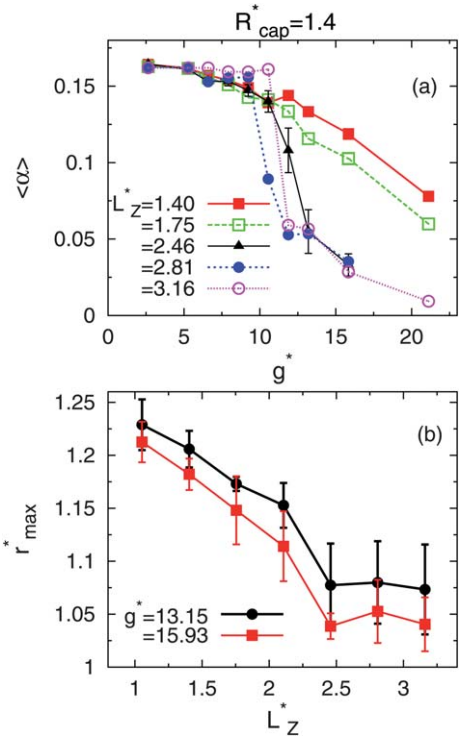

Fig. 3 (a) Average asphericity, $\langle\alpha\rangle$, at various RBC concentrations, $L_z/R_0 = 3.2$ to 1.4 (hematocrits $H_T = 0.12$ to 0.28), as a function of the pressure gradient, g^*, for $n_{ves} = 1$ and $R_{cap}/R_0 = 1.40$. (b) Maximum membrane radial extension, r_{max}/R_0, away from the capillary axis as a function of simulation (capillary) length (L_z/R_0).

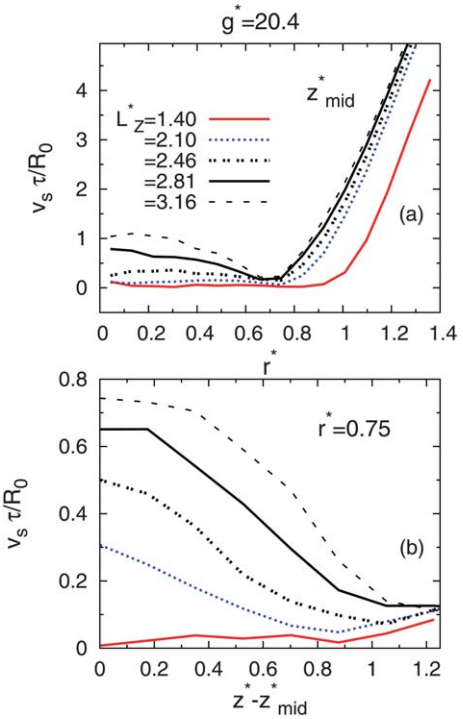

Fig. 5 Magnitude of the fluid velocity, $v_s = |\mathbf{v}_s|$, in the co-moving frame for a concentrated RBC suspension with $n_{ves} = 1$, $R_{cap}/R_0 = 1.40$, and various lengths, L_z/R_0. (a) v_s as a function of radial distance, r/R_{cap}, away from the capillary axis at the mid-plane, between an RBC and its mirror image, which is perpendicular to the z axis. (b) v_s as a function of distance $(z - z_{mid})/R_0$ parallel to the z axis from this mid-plane.

where $\langle\alpha\rangle$ goes from changing gradually to abruptly, corresponds to a cylinder length per cell in the range $1.8 < L_z/R_0 < 2.5$, which is slightly less than the capillary diameter of $2R_{cap}/R_0 = 2.8$. At separations between an RBC and its neighboring (image) cells greater than this 'critical length', the hydrodynamically mediated interaction between RBCs is too weak to influence the shape of the cells—they are 'hydrodynamically isolated'. We also observe that r_{max} levels off once the separation between nearest-neighbor cells exceeds $L_z^* = 2.0$ to 2.5. These results are consistent with the theoretical predictions obtained by solving the Stokes equation for the fluid flow about a periodic array of rigid model cells.[24–27] The fluid streamlines—denoted 'bolus' lines—in the cell co-moving frame, shown in Fig. 4, also appear qualitatively consistent with these predictions. Fluid velocities between RBCs are shown in Fig. 5. We find that the bolus vortices cease to exist for cell–cell separations in the range $1.4 < L_z/R_0 < 2.1$ (where the lower boundary equals R_{cap}/R_0); for these smaller separations, the fluid between the two RBCs becomes trapped and moves with the same velocity as the cells (see Fig. 5).

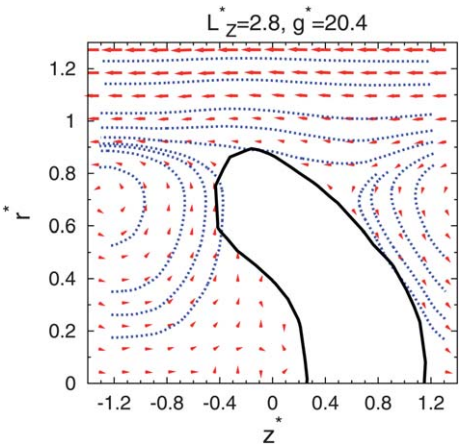

Fig. 4 Streamlines (dotted lines) and velocity field (arrows) in a reference frame co-moving with the RBC for $n_{ves} = 1$, $R_{cap}/R_0 = 1.40$, $L_z/R_0 = 2.8$, and $g^* = 20.4$. A sliced snapshot (solid contour) of the RBC is shown; a flow vortex ('bolus') is seen between RBCs. Within an RBC, the fluid flow velocity in this frame is zero; arrows are omitted from this interior space to emphasize the absence of a flow field.

4 Clustering of RBCs at low hematocrit

The study of clustering and correlations in the motion of RBCs, mediated by just hydrodynamic flows, requires simulations employing several elastic vesicles in the tube. We explore six ($n_{ves} = 6$) or three ($n_{ves} = 3$) cells in Sec. 4.1 and 4.2, respectively. For $n_{ves} = 6$, two capillary radii ($R_{cap}/R_0 = 1.40$ and 1.58) are studied with length $L_z/R_0 = 28$ (corresponding to $H_T = 0.084$ and 0.066, respectively). For $n_{ves} = 3$, the capillary radius $R_{cap}/R_0 = 1.40$ is investigated with length $L_z/R_0 = 14$ (corresponding to $H_T = 0.084$).

4.1 Six RBCs in a capillary

Fig. 6 shows subsequent snapshots of arrangements of RBCs in a capillary of radius $R_{cap}/R_0 = 1.58$ at $g^* > g_c^*$, where the cells are parachute shaped (see also Movie S2 in ESI†); Fig. 7 shows the corresponding trajectories (in a reference frame moving with the average flow velocity). Note that there are no direct contacts between any two adjacent cells. A comparison of these results with the corresponding data[50] for $R_{cap}/R_0 = 1.40$ shows that this clustering occurs very similarly for both capillary radii $R_{cap}/R_0 = 1.40$ and 1.58. In fast flow $g^* = 20.4$, RBCs form 6-cell clusters (the largest size of clusters possible in this system) for most of the simulation period (see Movie S1 in ESI†). In slower flow $g^* = 15.9$, clusters often break up and then reform into other clusters, as demonstrated in Fig. 6 and 7, and Movie S2 in ESI†.

Spatial pair correlations between the cells are characterized by the axial pair distribution function of the center-of-mass distances along the z direction,

$$G(z) = \frac{1}{n_{ves}\rho_B}\left\langle \sum_{i=1}^{n_{ves}} \sum_{j\neq i}^{n_{ves}} \delta(z - z_{ij}) \right\rangle, \quad (6)$$

where $z_{ij} = z_{cm,i} - z_{cm,j}$, $\rho_B = (n_{ves} - 1)/L_z$, and $\delta(z)$ is a smeared-out δ-function with $\delta(z) = 1/\Delta z$ for $z \in [-\Delta z/2, \Delta z/2]$ and 0 otherwise. Unless otherwise specified, $\Delta z^* = 0.03$. The correlation function is proportional to the conditional probability of finding the center-of-mass of one cell an axial distance z away from that of another cell. Alternatively, $\rho_B G(z)$ gives the effective RBC number density at a distance z away from a given cell.

Fig. 8 displays $G(z)$ for two flow velocities in the parachute phase at $R_{cap}/R_0 = 1.40$. Several pronounced peaks clearly show the existence of strong clustering; in contrast, just a single peak would indicate the formation of only RBC dimers. For comparison, we have also included in Fig. 8 the pair distribution function of a one-dimensional hard-sphere fluid[65,66] at thermal equilibrium, with the *same* line density $n_{hs}R_0/L_z = n_{ves}R_0/L_z = 0.214$ and a hard-sphere diameter $1.1R_0$, chosen so that the position of the first minimum in the hard-sphere pair distribution coincides with that of the first minimum in the RBC axial pair distribution at $g^* = 20.4$. Clearly, this hard-sphere fluid shows far less structure than our system of soft objects under flow.

Fig. 8(b) shows the probability of finding a cluster containing n_{cl} RBCs for the 6-cell system,

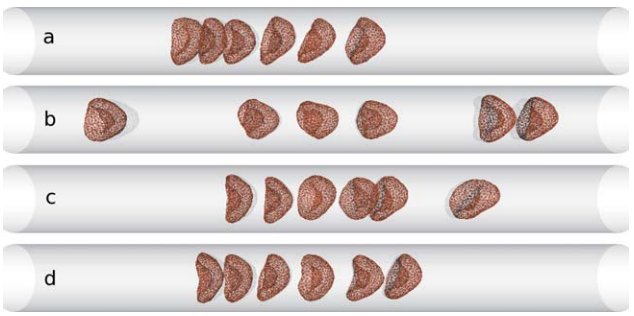

Fig. 6 Sequential snapshots taken during a simulation run with six cells ($n_{ves} = 6$) at $g^* = 15.9$ with $L_z/R_0 = 28$ and $R_{cap}/R_0 = 1.58$: (a) $t/\tau = 50$; (b) $t/\tau = 100$; (c) $t/\tau = 150$; and (d) $t/\tau = 200$.

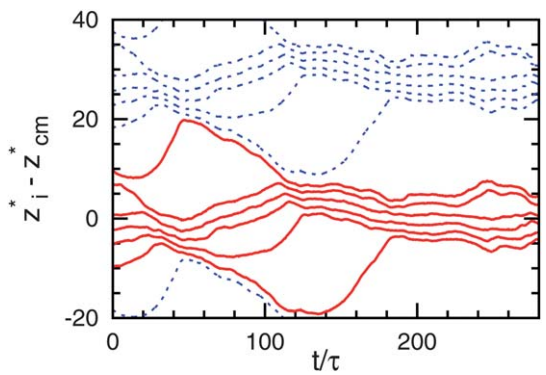

Fig. 7 Time development (during the same simulation run as Fig. 6) of the center-of-mass (cm) coordinates, $z_{cm,i}$, of six cells in the z direction in a dilute suspension with $n_{ves} = 6$, $L_z^* = L_z/R_0 = 28$, and $R_{cap}/R_0 = 1.58$. Trajectories are shown in a co-moving frame, *i.e.* relative to the center-of-mass $z_{cm} = (1/n_{ves})\sum_i z_{cm,i}$ of *all* cells. Solid and dashed lines represent the cm of RBCs and their periodic images, respectively.

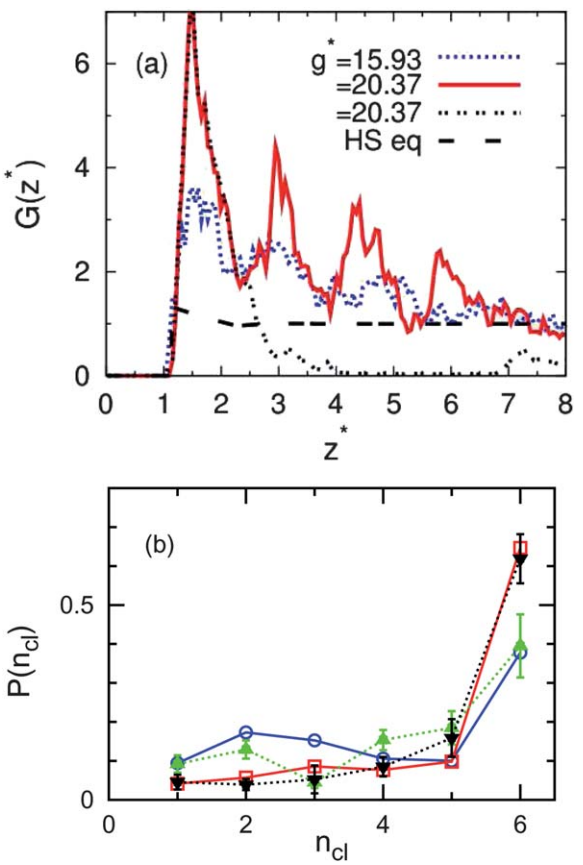

Fig. 8 (a) Axial pair distribution functions, $G(z)$, and (b) cluster-size probabilities, $P(n_{cl})$, for $n_{ves} = 6$, $L_z/R_0 = 28$. (a) The double-dot double-dot curve is the distribution function $G_{nn}(z)$ of center-of-mass distances of nearest-neighbor cells for $R_{cap}/R_0 = 1.40$. The $G(z)$ of a one-dimensional hard-sphere fluid at equilibrium (dashed line), a 'Tonk's gas', is included where these spheres have a diameter of $1.1R_0$. (b) $g^* = 15.93$ (○, △) and 20.37 (□, ∇) with $\varepsilon_1 = 3.5R_0$ (see text). Solid and dashed lines represent data at $R_{cap}/R_0 = 1.40$ and 1.58, respectively.

$$p(n_{cl}) = \frac{n_{cl} f(n_{cl})}{\sum_{n'_{cl}} n'_{cl} f(n'_{cl})}, \quad (7)$$

where $f(n'_{cl})$ is the total number of clusters of size n'_{cl} that appear during a simulation run. An RBC is defined to be part of a cluster if the axial center-of-mass distance to its nearest neighbor is less than a chosen distance $\varepsilon_1 = 3.5R_0$. This choice of ε_1 was made by considering the location where the contribution of *nearest-neighbor* pairs to $G(z)$ essentially disappears with increasing z^* (see Fig. 8(a)). The comparison of flows with $g^* = 15.9$ and $g^* = 20.4$ in Fig. 8 shows that the probability of finding smaller clusters is strongly reduced for faster flows in favor of larger clusters. Furthermore, Fig. 8 indicates that at the same pressure gradient (same g^*), the clustering behavior for the two capillary radii $R_{cap}/R_0 = 1.40$ and 1.58 is very similar, although small clusters of two or three cells appear a little more frequently for the smaller capillary radius.

4.2 Three RBCs in a capillary

To investigate the hydrodynamic interactions between RBCs in more detail, we have also simulated $n_{ves} = 3$ elastic vesicles in a capillary. Simulation snapshots, shown in Fig. 9, demonstrate the existence of a 3-cell cluster (see also Movie S3 in ESI†); as in the 6-cell case in Sec. 4.1, no direct contacts are observed between any two adjacent cells. Several simulations were performed at each g^* starting from different initial conditions with a total combined simulation time of about 2 to 3 $\times$ $10^3\tau$. The 3-cell clusters appear to be stable, particularly at the highest g^*, but infrequent 'orbiting' events occur where a 3-cell cluster breaks up into a 2-cell cluster and a 'free' cell which then orbits through the periodic boundary of the model capillary in a frame co-moving with the 2-cell cluster. In such orbiting events (a simulation snapshot is also shown in Fig. 9), the front cell of the 3-cell cluster separates from the cluster, ultimately becoming the back cell of a new 3-cell cluster (see Fig. 10), just as discussed for the cluster breakup and reformation in Sec. 4.1. The free RBC often appears during these events as a slipper, and moves fastest relative to the other RBCs when it has this shape. As g^* decreases, approaching g^*_c where an isolated RBC undergoes a parachute-to-discocyte transition (see Sec. 3.1), the frequency of such 'orbiting' events increases (see the inset of Fig. 11a).

The axial pair distribution functions, $G(z)$, of the distance between the centers of mass of pairs of cells is shown in Fig. 11. The high peaks demonstrate cluster formation. At $g^* = 20.4$, $G(z)$ of the distances between all pairs of RBCs (the full pair distribution function) has two peaks, while $G_{nn}(z)$, restricted to nearest-neighbor cells, has only a single peak. Thus, center-of-mass distances originating from nearest-neighbor pairs contribute to the first peak in $G(z)$ centered at $z/R_0 \simeq 2.6$, while only next-to-nearest neighbor distances contribute to the second peak centered at $z/R_0 \simeq 5.2$. On the other hand, at $g^* = 15.9$ and $g^* = 13.2$, $G(z)$ has *three* peaks, and $G_{nn}(z)$ for nearest neighbors has *two* peaks. This indicates that the 3-cell cluster has two possible internal states: a compact (CC) state and a loose (LL) state, with different nearest-neighbor distances in the z direction. Snapshots of these states are shown in Fig. 9; see also Movies S3 and S4 in ESI†.

There are two independent intra-cluster center-of-mass distances in a 3-cell cluster: the leftmost (l) $d_{3,l}$ and the rightmost (r) $d_{3,r}$ (see Fig. 9). In the CC state, $\langle d_{3,l}\rangle \simeq \langle d_{3,r}\rangle \simeq R_{cap}$ (with $R_{cap}/R_0 = 1.4$). These distances are relatively small, and are therefore designated by 'C' (for 'compact'); the magnitude in the variation of these distances is given by the width of the first peak

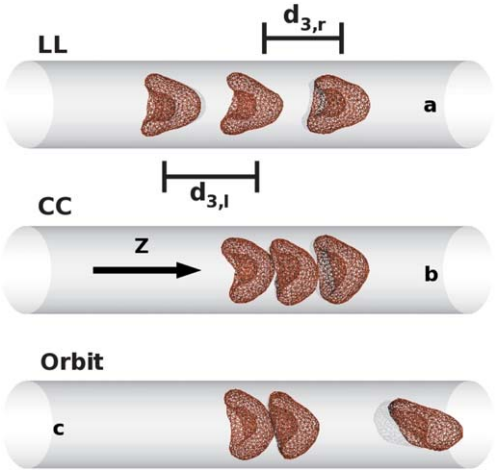

Fig. 9 Snapshots taken from simulations of a dilute suspension at $n_{ves} = 3$, $L_z/R_0 = 14$, and $R_{cap}/R_0 = 1.40$ ($H_T = 0.084$). (a) A loose (LL) 3-cell cluster at $g^* = 20.4$; see also Movie S3 in ESI†. Panels (b) and (c) show sequential snapshots taken from a simulation at $g^* = 13.2$; the front cell of a compact (CC) 3-cell cluster disjoints from the cluster, then orbits through the periodic boundary and becomes the back cell of a new 3-cell cluster; see also Movie S4 in ESI†. The rightmost and leftmost 3-cell intra-cluster center-of-mass (cm) distances are $d_{3,r}$ and $d_{3,l}$, respectively.

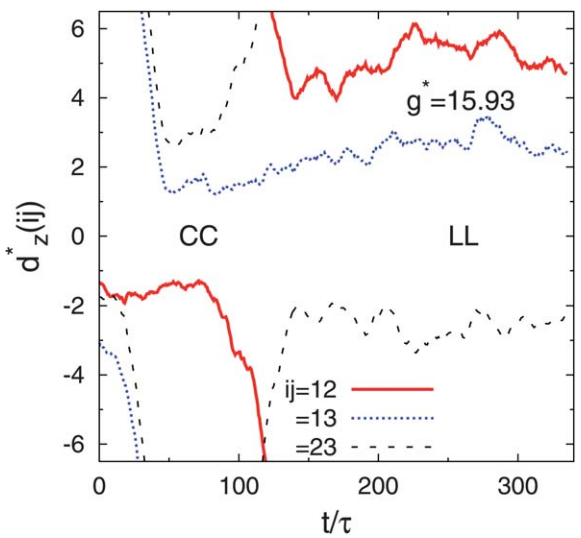

Fig. 10 Time development (during one simulation run) of the distances between the centers of mass (cm), z^*, of three RBCs in the z direction in a dilute suspension with $n_{ves} = 3$, $L^*_z = L_z/R_0 = 14$, and $R_{cap}/R_0 = 1.40$ ($H_T = 0.084$); here $d^*_z(ij) = z^*_{ij} - L^*_z \mathrm{nint}(z^*_{ij}/L^*_z)$ where $z^*_{ij} = z^*_i - z^*_j$. Two orbiting events are indicated by the curves going beyond the boundaries of this plot; the second such event results in a compact (CC) 3-cell cluster becoming a loose (LL) 3-cell cluster. The cells in the first 3-cell cluster are ordered as (123) = (lmr) where r is the front cell, m the middle, and l the back; the first orbiting event gives a new 3-cell cluster ordered as (312); then, the final event gives a loose 3-cell cluster ordered as (231).

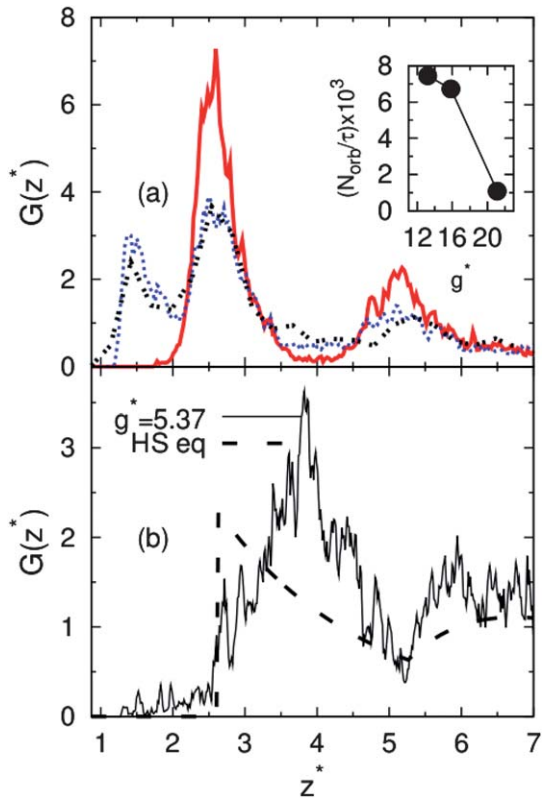

Fig. 11 (a) Axial pair distribution functions of the cells' center-of-mass separations at $n_{ves} = 3$, $L_z/R_0 = 14$, and $R_{cap}/R_0 = 1.40$ ($H_T = 0.084$). The inset gives the total number of orbiting events, N_{orb}, that occur during an intrinsic time τ; this number increases as g^* decreases. These orbiting events represent complete breaks of a 3-cell cluster into a 2-cell cluster and one 'free' cell. (b) Solid curve gives the axial pair distribution function at $g^* = 5.37$, where the RBCs existed only as discocytes; here no significant clustering was observed. The $G(z)$ of a one-dimensional hard-sphere fluid (dashed line) is included where these spheres have a diameter of $2.63R_0$.

of $G(z)$ at $g^* = 15.9$ and $g^* = 13.2$. In the LL state, $\langle d_{3,l}\rangle \simeq \langle d_{3,r}\rangle \simeq 2R_{cap}$. These distances are relatively large, and are therefore designated by 'L' (for 'loose'). At $g^* = 20.4$, the 3-cell cluster only exists in the LL state; furthermore, at $g^* = 15.9$ and $g^* = 13.2$, the 3-cell cluster spends more time in the LL state than in the CC state. 'Collisions' between RBCs after a complete orbit appear necessary in order to generate the compact state: transitions between the CC and LL states without a complete orbit never occurred.

The results for the cluster structure of small clusters differ from those for larger clusters described in Sec. 4.1. The most likely nearest-neighbor distance, z/R_0 10 : 5, for $n_{ves} = 6$ is close to that for the compact state of $n_{ves} = 3$. In addition, at $g^* = 20 : 4$, the width of the first peak in $G(z)$ for $n_{ves} = 6$ is much broader than this width for $n_{ves} = 3$. Thus, it seems that the C and L states can no longer be distinguished in clusters of many cells, and merge into a single state with larger distance fluctuations; this merging might be caused by the disturbance generated by the other cells in the cluster. For $g^* < g^*_c$, the RBCs are discocytes and show only a weak tendency to cluster: the first peak of $G(z)$ at $g^* = 5.4$, centered at $z \simeq 3.9R_0$ ($L_z^*/n_{ves} = 4.67$) is broad, and a second peak is not discernible (see Fig. 11). The pair distribution function of the one-dimensional hard-sphere fluid at equilibrium, with a line density $n_{hs}R_0/L_z = n_{ves}R_0/L_z = 0.214$ and hard-sphere diameter of $2.63R_0$ again shows far less structure than our system of soft objects under flow. Here, the choice of the hard-sphere diameter is again made such that the positions of the first minima of $G(z)$ for the hard-sphere fluid and the RBC suspension at $g^* = 5.4$ coincide.

To characterize the internal structure of the 3-cell clusters in more detail, we study correlations between the two nearest-neighbor distances in a cluster. Using a minimum-image convention with periodic boundary conditions along the z direction, we calculate three possible center-of-mass distances at any time during a simulation run. If any two of these distances are less than a distance ε_1, then we define that the cells form a 3-cell cluster. If any one of these distances is less than ε_1 and the minimum of the remaining two distances is greater than ε_2, then a 2-cell cluster is defined with one 'isolated' cell separated from this cluster. Noting the position where the first peak in $G(z_{nb})$ at $g^* = 20.37$ essentially ends with increasing z_{nb}, we set $\varepsilon_1 = 3.2R_0$ (somewhat smaller but nearly the same as in Sec. 4.1) and $\varepsilon_2 = 4.4R_0$, so that there is a clear distinction between a 2- and a 3-cell cluster.

The probability distributions of the single intra-cluster distance of a 2-cell cluster (not shown) indicate that the 2-cell cluster exists more often in a compact internal 'C' state. For most of the 2-cell clusters, the free RBC rejoins the 2-cell cluster to form a new 3-cell cluster through an orbiting event; however, for a small fraction, the free RBC leaves (farther than ε_2) but then returns to become again the front cell a 3-cell cluster.

Fig. 12 shows the distribution of the leftmost intra-cluster (LL) distances, $p(d_{3,l})$, for fixed $d_{3,r}$. As $d_{3,r}$ increases, the peak of $p(d_{3,l})$, shifts to larger $d_{3,l}$; thus, the two intra-cluster distances are strongly correlated.

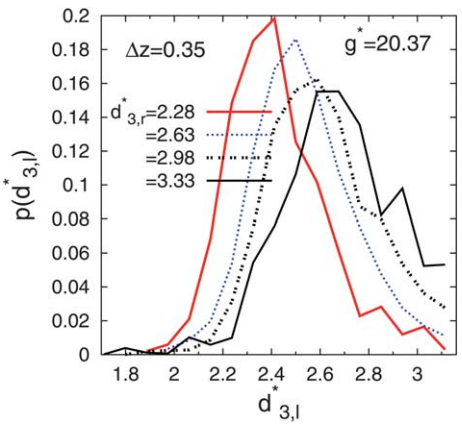

Fig. 12 Distributions of the leftmost intra-cluster distance, $d_{3,l}/R_0$, for different values of the rightmost intra-cluster distance, $d_{3,r}/R_0$. Parameters are $g^* = 20.4$, $n_{ves} = 3$, $L_z/R_0 = 14$, and $R_{cap}/R_0 = 1.40$. The bin sizes for $d_{3,r}$ and $d_{3,l}$ are given by $\Delta z/R_0 = 0.35$ and 0.088, respectively; these bin sizes are chosen to produce adequate statistics and a sufficiently smooth curve, respectively. These choices are not unique; for example, shifts in $p(d_{3,l})$ are also observed using a twice as large bin size $\Delta z/R_0 = 0.7$ for $d_{3,r}$.

To extract information about the probabilities of the CC and LL internal states to occur in a 3-cell cluster, we use ranges guided by the widths and positions of the first and second peaks of $G(z)$ for $g^* = 15.9$ and $g^* = 13.2$ in Fig. 11(a). If $d_{3,l}/R_0 < 1.9$ and $d_{3,r}/R_0 < 1.9$, then the CC state exists; if $d_{3,l}/R_0 > 1.9$ and $d_{3,r}/R_0 > 1.9$, then the LL state exists. The sum of the fractions of time spent in the CC and LL states is less than unity because there exists a remaining internal state characterized by a small and a large intra-cluster distance; however, this hybrid CL state appears not to exist as metastable state for any appreciable length of time. The 3-cell cluster spends 40% to 60% of its time in the LL state and only 10% to 20% of its time in the CC state for $g^* = 15.9$ and $g^* = 13.2$ (the error here is only a crude estimate obtained by dividing the total simulation time into three equally sized blocks). All transitions between compact and loose states proceeded through intervening 'orbiting' events; in addition, more orbiting events were seen from an CC state than from the LL state; as a result, the 2-cell cluster inherits its compact state from the compact (CC) 3-cell cluster from which the 2-cell cluster is 'born'.

Fig. 13 displays the probability distributions for the average RBC velocity, v_{ves}, at $g^* = 15.9$ for a 2- and a 3-cell clusters, as well as for a single, 'orbiting' cell separated from a 2-cell cluster; v_{ves} is an instantaneous average taken over each of the cells of a particular cluster species. The free cell moves on average with the largest velocity, followed by the 3-cell cluster and then the 2-cell cluster. Thus, the free cell can catch up with the 2-cell cluster. Fig. 13 also shows the distribution $p(r^*_{max})$ of maximum radial extension of the cell membrane from the capillary axis for the 3-cell cluster It has two peaks, one at lower and another at higher r^*_{max}, which correspond to the internal LL and CC states, respectively. The different peak heights reflect the fact that the 3-cell cluster spends more time in the LL than in the CC state.

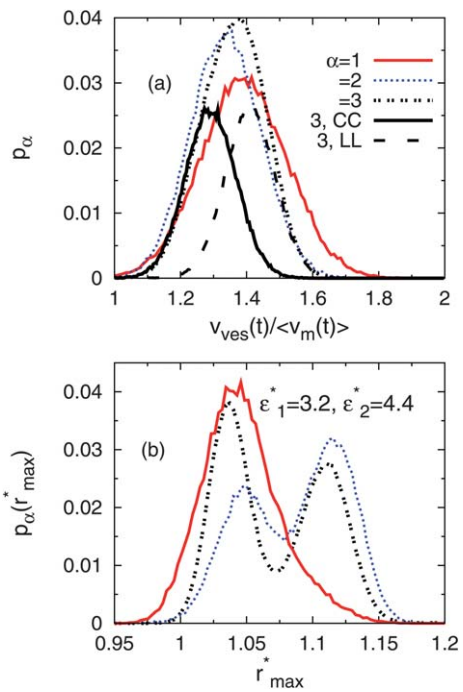

Fig. 13 (a) Velocity, v_{ves}, and (b) maximum membrane radial extension, r_{max}, probability distributions for a single cell ($\alpha = 1$), a 2-cell cluster ($\alpha = 2$), and a 3-cell cluster ($\alpha = 3$) at $g^* = 15.9$ with $n_{ves} = 3$, $L_z/R_0 = 14$, and $R_{cap}/R_0 = 1.40$. Panel (a) also gives the velocity distributions for a 3-cell cluster in the loose (LL) and compact (CC) internal states. The separation distances, $\varepsilon_1/R_0 = 3.2$ and $\varepsilon_2/R_0 = 4.4$, are used to define the clusters. The relative, qualitative appearance of all these distributions at $g^* = 13.2$ is the same.

4.3 Discussion

Based on our results for the $n_{ves} = 3$ system, we can now discuss the mechanism of deformation-induced clustering of RBCs. The RBCs form parachutes in a cluster for $g^* > g^*_c$, but the RBC shape depends on the distance between neighboring cells. As the cells come closer to each other within the 3-cell cluster, the neighboring cells are more shielded from the shear forces of the fluid, and $\langle r_{max} \rangle$ increases; then, the 3-cell cluster flows more slowly and its pressure drop increases, because the cluster acts more like a plug to fluid flow (see Fig. 13). A similar shape change occurs in the dense suspension with $n_{ves} = 1$ (see Sec. 3); there, the neighboring distance is exactly L_z due to the periodic boundary conditions. The RBC asphericity α shows a jump at $L_z/R_0 \simeq 2$ and $g^* \geq 13.2$ (see Fig. 3). This distance coincides with the position $2R_0$ where the first peak in $G(z)$ at $g^* = 13.2$ and $g^* = 15.9$ ends and the second peak begins; this position marks the border between what we have defined as a compact (C) or a loose

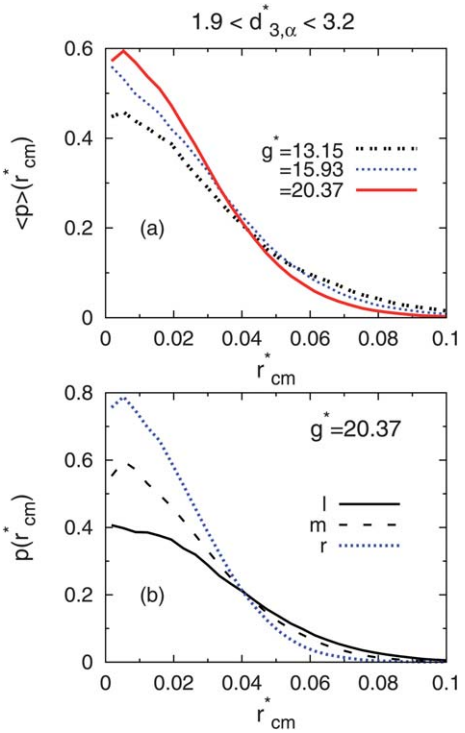

Fig. 14 Distributions of the RBC center-of-mass radial position, r_{cm}/R_0, for a 3-cell cluster in the loose (LL) internal state [$1.9 < d_{3,\alpha}/R_0 < 3.2$] at $g^* = 20.4$, $n_{ves} = 3$, $L_z/R_0 = 14$, and $R_{cap}/R_0 = 1.40$. Distributions were obtained by dividing raw histograms by $2\pi r_{cm}$. (a) Average distribution of r_{cm} averaged over the three individual cell distributions. (b) Distribution functions for the radial positions $r_{cm,i}$, with $i \in$ {l,m,r}, for individual RBCs (where 'l', 'm', and 'r' represent the left, middle, and right cell within the cluster). The relative displacement/shift between the l, m, and r distributions were also observed at $g^* = 15.9$ and 13.1.

(L) nearest-neighbor intra-cluster distance. Thus, the compact state is related to this shape transition from a parachute with a deep dimple to one with a shallow dimple.

In capillary flow, hydrodynamic lift forces cause cell migration away from the wall to the capillary axis.[67–72] As g^* decreases, the magnitude of the lift force decreases. Our simulation results for $g^* > g_c^*$ indicate that fluctuations in RBC shapes and positions at low g^* are indeed more pronounced than at high g^*. This is demonstrated in Fig. 14(a), where the distribution of radial distances r_{cm} of the cell's center of mass becomes more centered near the capillary axis with increasing flow velocity. When an RBC with a parachute shape shifts away from the capillary axis, there is an increased chance that it will be deformed into a slipper shape; this is the shape most often adopted by the front cell of the 3-cell cluster when it breaks free and executes an orbit of the simulation cylinder. However, not all fluctuations in the RBC center of mass off-axis result in such drastic shape transformations into a slipper shape. Fig. 14(b) shows distributions for the radial center-of-mass position $r_{cm,i}$, with $i \in \{l,m,r\}$, for the three individual cells within a LL 3-cell cluster. The back (l) cell in the 3-cell cluster has larger fluctuations in the position of its center of mass off-axis than the middle (m) cell and the front (r) cell of this cluster. Interestingly, within the LL state at all g^* considered, $\langle r_{max}(l)\rangle \gtrsim \langle r_{max}(m)\rangle \gtrsim \langle r_{max}(r)\rangle$, $\langle l_{max}(l)\rangle \lesssim \langle l_{max}(m)\rangle \lesssim \langle l_{max}(r)\rangle$, and $\langle d_{3,l}\rangle \lesssim \langle d_{3,r}\rangle$. The origin of this behavior is the asymmetric parachute shape, which is more pointed in front and more broad in the back; this shape implies that also the fluid velocity profile is more parabolic before and more plug-like behind each cell, so that the leading cell of the cluster is pulled more to the center, whereas the trailing cell can move more easily sideways and have larger fluctuations away from the capillary axis.

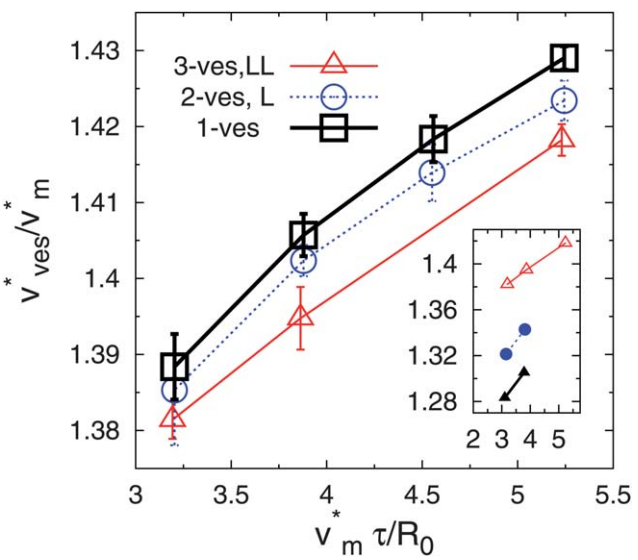

Fig. 15 Vesicle velocities for a loose (LL) 3-cell cluster, as well as a loose (L) 2-cell cluster and a single 'steady-state' cell (1-ves). The three curves were obtained from simulations with three, two, and one cell per simulation cylinder all at $H_T = 0.084$ with $R_{cap}/R_0 = 1.40$. Inset compares the RBC velocity of a LL 3-cell cluster to the velocities of a compact (C) 2-cell cluster (solid circles) (obtained from during an orbiting event at $n_{ves} = 3$ and $H_T = 0.084$) and a compact (CC) 3-cell cluster (solid triangles).

We have found that two mechanisms are at play in stabilizing RBC clusters, the effective hydrodynamic attraction induced by the bolus flow (see Sec. 3.2), and the different flow velocities of single cells and cell clusters. The simulated cell suspension is dilute ($H_T = 0.084$). Since a free RBC during an orbiting event, where it often appears as a slipper, flows faster than a compact 2-cell cluster, a free cell can catch up to the cluster before it had time to relax to its average parachute shape. In the limit of even higher dilution, small clusters with $n_{ves} = 3$, which are initially isolated, should have sufficient time to be able to relax to their steady LL state; then, cluster formation might be governed by the differences in the mean velocity of the isolated clusters. Therefore, we show in Fig. 15 the mean cluster velocity, v_{ves} *versus* mean fluid flow velocity, v_m, for several different cluster species obtained from simulations with three, two, and one elastic vesicles per simulation cylinder at the same hematocrit, $H_T = 0.084$, and with $R_{cap}/R_0 = 1.40$. Compared to the velocities of the compact 2- or 3-cell clusters (see the inset of Fig. 15), the differences in the velocities of a single (steady state) cell, loose 2-, and loose 3-cell clusters are very small. Therefore, we suspect that in a very dilute suspension, cell clustering could occur, but very slowly (compared to the formation of clusters that occurs during an orbiting event), because of the small velocity differences between the different loose cluster species and the large distances between any two nearest-neighbor clusters.

5 Summary and conclusions

We have studied the transition from a discocyte to a parachute shape of elastic vesicles and their clustering behavior in microcapillary flows. The discocyte-to-parachute transition reduces the flow resistance. Hydrodynamic interactions coupled with RBC deformations induce clustering in the regime of higher flow velocities, where parachute shapes prevail.

For small cluster sizes, the cell clusters can show two internal states, compactly and loosely packed RBCs with parachute shapes of shallow and deep dimples, respectively. Two critical distances, Δz_1 and Δz_2 (with $\Delta z_1 < \Delta z_2$), mark the boundaries between different levels of hydrodynamic interaction. For distances larger than Δz_2, cells are hydrodynamically isolated and do not interact. Δz_1 is the boundary where the shapes of two neighboring cells cease to be independent; in addition, for distances less than Δz_1, the bolus-flow structure between neighboring RBCs disappears. Therefore, changes in flow structure are strongly correlated with changes in RBC shape. These critical distances are the locations where the first peak in the axial pair distribution function for the compact and loose clusters essentially disappear with increasing nearest-neighbor distance. For larger cluster sizes, two distinct internal states do not appear possible because of complex interactions (hydrodynamic flows coupled to thermal fluctuations) with the other cells.

The clustering of RBCs seen in experiments of blood flow through a glass capillary[8] and the narrow arterioles of a rabbit[73] have been explained based on the polydispersity of a blood sample, where RBCs show a variation in size and flexibility. The membranes of more flexible cells can more easily deform, becoming closer to the capillary axis; as a result, these flexible cells can move faster and crowd behind the more slow moving, inflexible cells. We have shown that clustering can occur even in

a monodisperse suspension of RBCs that are identical in their size and flexibility. Similar clustering is expected for other soft objects such as liquid droplets and lipid vesicles.

In slow blood flow, fibrinogen induces RBCs aggregation called 'rouleaux', where the RBCs adhere like a stack of coins.[11,74] Subjected to sufficiently large shear gradients, the RBC rouleaux break-up and disperse in flow.[75] Therefore, it will be interesting in the future to study the clustering of elastic vesicles as model RBCs in the presence of attractive membrane interactions in capillary flows.

Acknowledgements

We thank I. O. Götze, T. Auth, M. Ripoll, G. Vliegenthart, and R. G. Winkler for helpful discussions. Support of this work by the DFG through the priority program SPP1164, 'Nano- and Microfluidics', is gratefully acknowledged.

References

1 H. A. Stone, *Annu. Rev. Fluid Mech.*, 1994, **26**, 65–102.
2 A. Walter, H. Rehage and H. Leonhard, *Colloids Surf., A*, 2001, **183**, 123–132.
3 R. Finken and U. Seifert, *J. Phys.: Condens. Matter*, 2006, **18**, L185–191.
4 V. Kantsler, E. Segre and V. Steinberg, *Phys. Rev. Lett.*, 2007, **99**, 178102.
5 K. S. Turitsyn and S. S. Vergeles, *Phys. Rev. Lett.*, 2008, **100**, 028103.
6 V. Vitkova, M. Mader and T. Podgorski, *Europhys. Lett.*, 2004, **68**, 398.
7 R. Skalak, *Science*, 1969, **164**, 717.
8 P. Gaehtgens, C. Dührssen and K. H. Albrecht, *Blood Cells*, 1980, **6**, 799–812.
9 Y. Suzuki, N. Tateishi, M. Soutani and N. Maeda, *Microcirculation*, 1996, **3**, 49.
10 K. Tsukada, E. Sekizuka, C. Oshio and H. Minamitani, *Microvasc. Res.*, 2001, **61**, 231.
11 Y. C. Fung, *Biomechanics: circulation*, Springer, New York, 2nd edn, 1997.
12 N. Mohandas and E. Evans, *Annu. Rev. Biophys. Biomol. Struct.*, 1994, **23**, 787–818.
13 M. Dao, C. T. Lim and S. Suresh, *J. Mech. Phys. Solids*, 2003, **51**, 2259–2280.
14 Y. C. Fung, *Biomechanics: mechanical properties of living tissues*, Springer, Berlin, 2nd edn, 2004.
15 J. P. Shelby, J. White, K. Ganesan, P. K. Rathod and D. T. Chiu, *Proc. Natl. Acad. Sci. U. S. A.*, 2003, **100**, 14618–14622.
16 J. Li, G. Lykotrafitis, M. Dao and S. Suresh, *Proc. Natl. Acad. Sci. U. S. A.*, 2007, **104**, 4937–4942.
17 J. M. Higgins, D. T. Eddington, S. N. Bhatia and L. Mahadevan, *Proc. Natl. Acad. Sci. U. S. A.*, 2007, **104**, 20496–20500.
18 R. S. Sprague, M. L. Ellsworth, A. H. Stephenson and A. J. Lonigro, *Am.J. Physiol.*, 2001, **281**, C1158–C1164.
19 J. Carroll, M. Raththagala, W. Subasinghe, S. Baguzis, T. D. Oblak, P. Root and D. Spence, *Mol. BioSyst.*, 2006, **2**, 305–311.
20 R. Fåhraeus, *Physiol. Rev.*, 1929, **9**, 241.
21 R. Fåhraeus and T. Lindqvist, *Am. J. Physiol.*, 1931, **96**, 562.
22 M. Abkarian, C. Lartigue and A. Viallat, *Phys. Rev. Lett.*, 2002, **88**, 068103.
23 R. Whitmore, *J. Appl. Physiol.*, 1967, **22**, 767.
24 H. Wang and R. Skalak, *J. Fluid Mech.*, 1969, **38**, 75.
25 T. Chen and R. Skalak, *Appl. Sci. Res.*, 1970, **22**, 403.
26 H. Lew and Y. Fung, *Biophys. J.*, 1970, **10**, 80.
27 R. Skalak, P. Chen and S. Chien, *Biorheology*, 1972, **9**, 67.
28 B. Cui, H. Diamant and B. Lin, *Phys. Rev. Lett.*, 2002, **89**, 188302.
29 H. Diamant, *J. Phys. Soc. Jpn.*, 2009, **78**, 041002.
30 R. Skalak, *Biorheology*, 1990, **27**, 277–293.
31 T. Secomb, R. Skalak, N. Ozkaya and J. Gross, *J. Fluid Mech.*, 1986, **163**, 405.
32 R. Bruinsma, *Phys. A*, 1996, **234**, 249.
33 C. Queguiner and D. Barthes-Biesel, *J. Fluid Mech.*, 1997, **348**, 349.
34 C. Pozikidis, *Ann. Biomed. Eng.*, 2005, **33**, 165.
35 C. Pozikidis, *Phys. Fluids*, 2005, **17**, 031503.
36 Y. Liu and W. Liu, *J. Comput. Phys.*, 2006, **220**, 139.
37 M. Dupin, I. Halliday, C. Care, L. Alboul and L. Munn, *Phys. Rev. Lett.*, 2007, **75**, 066707.
38 W. Dzwinel, K. Boryezko and D. A. Yuen, *J. Colloid Interface Sci.*, 2003, **258**, 163.
39 H. Noguchi and G. Gompper, *Proc. Natl. Acad. Sci. U. S. A.*, 2005, **102**, 14159.
40 D. A. Fedosov, B. Caswell and G. E. Karniadakis, *Biophys. J.*, 2010, **98**, 2215–2225.
41 A. Malevanets and R. Kapral, *J. Chem. Phys.*, 1999, **110**, 8605.
42 R. Kapral, *Adv. Chem. Phys.*, 2008, **140**, 89–146.
43 G. Gompper, T. Ihle, D. M. Kroll and R. G. Winkler, *Adv. Polym. Sci.*, 2009, **221**, 1–87.
44 H. Noguchi, N. Kikuchi and G. Gompper, *Europhys. Lett.*, 2007, **78**, 10005.
45 T. Ihle and D. M. Kroll, *Phys. Rev. E: Stat. Phys., Plasmas, Fluids, Relat. Interdiscip. Top.*, 2001, **63**, 020201(R).
46 H. Noguchi and G. Gompper, *Phys. Rev. Lett.*, 2004, **93**, 258102.
47 H. Noguchi and G. Gompper, *Phys. Rev. E: Stat., Nonlinear, Soft Matter Phys.*, 2005, **72**, 011901.
48 H. Noguchi and G. Gompper, *Phys. Rev. Lett.*, 2007, **98**, 128103.
49 H. Noguchi, G. Gompper, L. Schmid, A. Wixforth and T. Franke, *Europhys. Lett.*, 2010, **89**, 28002.
50 J. L. McWhirter, H. Noguchi and G. Gompper, *Proc. Natl. Acad. Sci. U. S. A.*, 2009, **106**, 6039–6043.
51 S. Chien, *Science*, 1970, **168**, 977–979.
52 G. Gompper and D. M. Kroll, *J. Phys.: Condens. Matter*, 1997, **9**, 8795–8834.
53 G. Gompper and D. M. Kroll, *Statistical Mechanics of Membranes and Surfaces*, World Scientific, Singapore, 2nd edn, 2004, pp. 359–426.
54 D. Discher, D. Boal and S. Boey, *Biophys. J.*, 1998, **75**, 1584.
55 H. Lim, M. Wortis and R. Mukhopadhyay, *Proc. Natl. Acad. Sci. U. S. A.*, 2002, **99**, 16766.
56 W. Helfrich, *Z. Naturforsch.*, 1973, **28c**, 693.
57 G. Gompper and D. M. Kroll, *J. Phys. I*, 1996, **6**, 1305–1320.
58 P. Canham and A. Burton, *Circ. Res.*, 1968, **22**, 405.
59 K. Engstrom and E. Lofvenberg, *Blood*, 1998, **91**, 3986.
60 A. Lamura, G. Gompper, T. Ihle and D. Kroll, *Europhys. Lett.*, 2001, **56**, 319.
61 M. Ripoll, K. Mussawisade, R. G. Winkler and G. Gompper, *Europhys. Lett.*, 2004, **68**, 106–112.
62 G. Tomaiuolo, M. Simeone, V. Martinelli, B. Rotoli and S. Guido, *Soft Matter*, 2009, **5**, 3736–3740.
63 B. Kaoui, G. Biros and C. Misbah, *Phys. Rev. Lett.*, 2009, **103**, 188101.
64 J. Rudnick and G. Gaspari, *J. Phys. A: Math. Gen.*, 1986, **19**, L191–L193.
65 L. Tonks, *Phys. Rev.*, 1936, **50**, 955.
66 Z. Salsburg, R. Zwanzig and J. Kirkwood, *J. Chem. Phys.*, 1953, **21**, 1098.
67 P. Olla, *Phys. Rev. Lett.*, 1999, **82**, 453.
68 I. Cantat and C. Misbah, *Phys. Rev. Lett.*, 1999, **83**, 880.
69 S. Sukumaran and U. Seifert, *Phys. Rev. E: Stat. Phys., Plasmas, Fluids, Relat. Interdiscip. Top.*, 2001, **64**, 011916.
70 M. Abkarian and A. Viallat, *Biophys. J.*, 2005, **89**, 1055.
71 B. Kaoui, G. Ristow, I. Cantat, C. Misbah and W. Zimmermann, *Phys. Rev. E: Stat., Nonlinear, Soft Matter Phys.*, 2008, **77**, 021903.
72 S. Messlinger, B. Schmidt, H. Noguchi and G. Gompper, *Phys. Rev. E: Stat., Nonlinear, Soft Matter Phys.*, 2009, **80**, 011901.
73 P. Monro, *Biorheology*, 1963, **1**, 239.
74 D. Voet and J. Voet, *Biochemistry*, Wiley, New York, 1995.
75 D. Fedosov, W. Pan, B. Caswell, G. Gompper and G. E. Karniadakis, *Proc. Natl. Acad. Sci. U. S. A.*, 2011, **108**, 11772–11777.